Lab on a Chip

Dynamic formation of a microchannel array enabling kinesin-driven microtubule transport between separate compartments on a chip†

Kazuya Fujimoto,[a] Moeto Nagai,[b] Hirofumi Shintaku,[a] Hidetoshi Kotera[a] and Ryuji Yokokawa*[a]

Microtubules driven by kinesin motors have been utilised as "molecular shuttles" in microfluidic environments with potential applications in autonomous nanoscale manipulations such as capturing, separating, and/or concentrating biomolecules. However, the conventional flow cell-based assay has difficulty in separating bound target molecules from free ones even with buffer flushing because molecular manipulations by molecular shuttles take place on a glass surface and molecular binding occurs stochastically; this makes it difficult to determine whether molecules are carried by molecular shuttles or by diffusion. To address this issue, we developed a microtubule-based transport system between two compartments connected by a single-micrometre-scale channel array that forms dynamically via pneumatic actuation of a polydimethylsiloxane membrane. The device comprises three layers—a control channel layer (top), a microfluidic channel layer (middle), and a channel array layer (bottom)—that enable selective injection of assay solutions into a target compartment and dynamic formation of the microchannel array. The pneumatic channel also serves as a nitrogen supply path to the assay area, which reduces photobleaching of fluorescently labelled microtubules and deactivation of kinesin by oxygen radicals. The channel array suppresses cross-contamination of molecules caused by diffusion or pressure-driven flow between compartments, facilitating unidirectional transport of molecular shuttles from one compartment to another. The method demonstrates, for the first time, efficient and unidirectional microtubule transport by eliminating diffusion of target molecules on a chip and thus may constitute one of the key aspects of motor-driven nanosystems.

Introduction

Since the proposal of micro total analysis systems (μTAS) or lab-on-a-chip,[1] control of fluidic samples in micrometer-scale environments has advanced rapidly due to the utilisation of microfabrication techniques.[2] Various functional microfluidic devices have been developed for chemical analysis, medical diagnosis, and other purposes, demonstrating their advantages such as small sample volume and short assay time.[3] Although pressure-driven flow is prevalent in molecular manipulations in μTAS applications, direct manipulation of target molecules is also important for further downsizing of devices because handling extremely small volumes of solution is challenging when pressure-driven flow is used. Therefore,

electrokinetic manipulation of molecules by external fields has been extensively studied for the purpose of concentrating or separating molecules.[4–6]

In the last decade, many researchers have established novel molecular transport schemes via the use of motor proteins. Motor proteins directly convert chemical energy into mechanical work on the molecular scale, implying that nanosystems can be supported by autonomous motor-driven manipulations.[7] The motor protein system comprising kinesin (motor) and microtubules (MTs) plays important roles in intracellular vesicular transport and in regulating cell division in eukaryotes.[8,9] Amongst the various artificial motor protein systems used currently, the combination of kinesin/MTs is widely used in a geometry called "gliding assay" in which MTs glide on a kinesin-coated surface.[10,11] Regarding MTs as "molecular shuttles", molecules can be directly carried on MTs and transported by kinesin motility via ATP hydrolysis in vitro. The integration of micro/nano-fabrication and molecular bionanotechnology makes it possible to load/unload and control the direction of molecular transport. Various binding mechanisms have been employed for cargo loading

[a] Department of Micro Engineering, Kyoto University, Kyoto-daigaku Katsura, Nishikyo-ku, Kyoto, 615-8540, Japan. E-mail: ryuji@me.kyoto-u.ac.jp
[b] Department of Mechanical Engineering, Toyohashi University of Technology, 1-1 Hibarigaoka, Tempaku-cho, Toyohashi, Aichi, 441-8580, Japan

onto MTs, such as biotin–streptavidin interaction,[12] DNA hybridisation,[13–16] and antigen–antibody recognition.[17–19] Both the direction and location of molecular gliding have been controlled by microfabricated structures,[20–24] and/or by applying external forces such as an electric field,[25–28] magnetic field,[29] and shear flow.[30–32] Recently, polymer patterning on a substrate for selective immobilisation of kinesin has also been reported.[33–35] Moreover, integration of cargo loading and subsequent control of transport direction have demonstrated the utility of molecular shuttles in achieving molecular separation or concentration.[36,37]

The next challenge in molecular shuttle applications is to realise autonomous sample processing relying on fewer external manipulations such as sequential exchange of solutions. Bachand *et al.* proposed a device concept consisting of multiple separate modules, in which MTs autonomously and sequentially carry target molecules from the loading module to the tagging and detection modules.[38] In this concept, target molecules must be transported across separate modules filled with different solutions without cross-contamination. However, such molecular transport is not trivial because

injecting solutions into individual modules is extremely challenging and diffusion of molecules causes cross-contamination. Kim *et al.* tackled this issue using laminar flow sandwiched by two sheath flows, where streptavidin molecules were captured on biotin-labelled MTs and concentrated.[39] More recently, Steuerwald *et al.* have also utilised laminar flows to sequentially load streptavidin and DNA molecules onto MTs *via* their gliding in two adjacent flows—one flow containing streptavidin and the other containing DNA.[40] MT gliding across separate regions has been thus reported by utilising continuous laminar flows, but several shortcomings hamper the fabrication of a more functional device. Most importantly, identifying the driving force of nanotransport of target molecules remains challenging because it is not easy to segregate active transport of molecular shuttles from diffusion-mediated transport and pressure-driven flow in a flow cell-based assay. In addition, laminar flow needs to be maintained throughout the assay *via* laborious external control using syringe pumps. A high flow rate causes MT detachment from the device surface, thereby decreasing the efficiency of transport.[40]
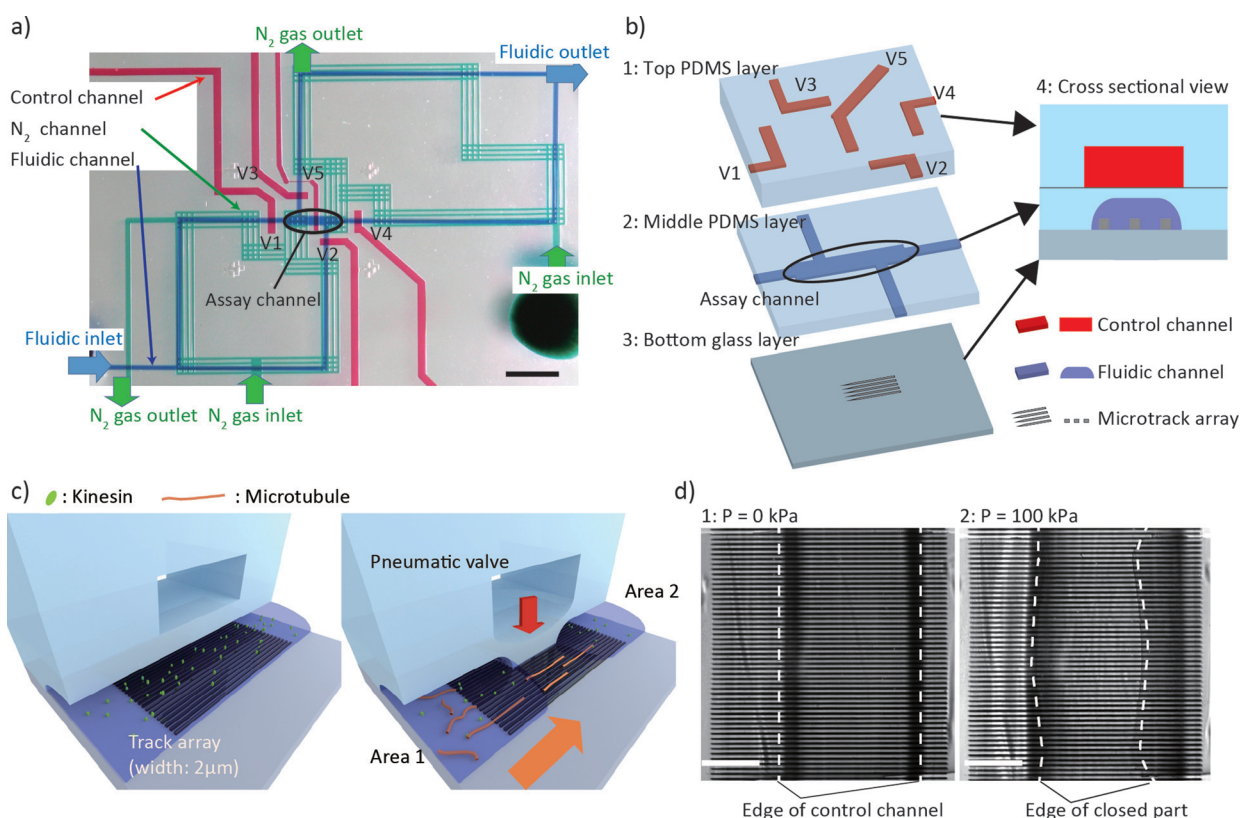

Fig. 1 Fabricated device and its functions. a) Overview of the device. Control channel, fluidic channel, and N_2 channel are coloured red, blue, and green, respectively. The microtrack array patterned on the glass cover slip is located at the centre (enclosed by a circle). Scale bar is 2 mm. b) Three-layer microfluidic device. b-1) Control channels (red) are fabricated on the top PDMS layer. b-2) Fluidic channels (blue) are moulded on the second PDMS layer, of which the channel top is composed of a thin PDMS membrane for pneumatic actuation. b-3) Microtrack array (gray) is patterned on a glass cover slip. b-4) These three layers are bonded together as illustrated. c) Schematic of dynamic formation of a microchannel array. After kinesin molecules are immobilised on the glass surface, the top PDMS membrane is pneumatically actuated, resulting in the formation of the closed channel array. d-1) The microtrack array aligned to a control channel. Without applied pressure, the edges of the control channel are clearly observed (white dotted lines). d-2) With an applied pressure of 100 kPa, the PDMS membrane is compressed to form the channel array. White dotted lines indicate the boundary of the closed area. Scale bar is 50 μm.

Here, we propose a microfluidic system that enables MT-based transport between two compartments which are physically separated. We used a three-layer microfluidic device to assay MTs under fluidically static conditions without pressure-driven flow (Fig. 1a, b). The device enables MTs to glide between physically separate compartments (area 1 and area 2) through a single-micrometre-scale channel array while eliminating diffusion of cargo molecules or MTs in bulk solution. Selective injection of buffer solutions by pneumatic valves and high fluidic resistance keep distinct sets of molecules in two separate compartments. Pneumatic channels were also utilised to supply nitrogen gas to extend the lifetimes of MTs and kinesin.

Materials and methods

Design of the microfluidic device

The device is constructed of two poly(dimethylsiloxane) (PDMS) layers and a bottom glass cover slip (Fig. 1b). Control channels in the top PDMS layer (Fig. 1b-1) actuate thin PDMS membranes in the middle layer (Fig. 1b-2) to control the direction of buffer solution flow, as reported.[41,42] In addition to such conventional use of pneumatic control channels, they have two unique functions in our device. First, one of the control channels serves to dynamically create the channel array during assay by compressing the PDMS membrane on the microtrack array fabricated on the cover slip (Fig. 1b-3, -4, and c). Quick and easy formation of the channel array facilitates easy buffer perfusions with less hydraulic resistance before forming the channel array. This method promotes MT gliding in the single-micrometre-scale channel array of 2 μm width and ~0.7 μm height, a channel size that has made assays laborious due to a large pressure drop.[43–46] Second, nitrogen gas (N_2) is supplied to the assay channel area, which extends the assay time by reducing photobleaching and protein deactivation via reaction with oxygen radicals.[47]

Microfluidic device fabrication

Top PDMS layer with control channels. A mould for control channels was fabricated by UV photolithography of an SU-8 3050 resist (MicroChem) on a silicon substrate (see the ESI† for details of mould fabrication). A PDMS prepolymer mixed with a curing agent (SILPOT 184W/C, Dow Corning Toray) at a ratio of 10:1 (w/w) was cast on the mould with a thickness of ~10 mm. It was degassed in a vacuum chamber for 1 h, cured at 80 °C for 1 h, and removed from the mould. Inlet and outlet holes used for the external pressure source and N_2 supply were punched using a biopsy punch (Sterile Dermal Biopsy Punch, 3 mm, Kai Industries).

Middle PDMS layer with fluidic channels sealed by a thin PDMS membrane. An AZP4903 (AZ Electronic Materials) photoresist patterned on a silicon substrate was employed as the mould for fluidic channels. Following the photolithography process, the photoresist was reflowed at 150 °C for 2 h to produce round cross-sections. The dimensions of the resulting resist shapes were measured by using a surface profilometer (Dektak XT-S, Veeco) before and after reflow (Fig. S1†), and finite element model simulation with Mems-ONE software (Micromachine Centre, Japan) was conducted to examine if the round cross-sections were suitable for valve closure[48] (Fig. S2†). A PDMS prepolymer and a curing agent were mixed at a ratio of 20:1, and 0.2 g of a wetting agent (501W additive, Dow Corning) per 10 g of mixture was added. The mixture was spin-coated on the mould at 2000 rpm for 60 s (K359S1, Kyowariken) to obtain a 60 μm-thick PDMS membrane that was then cured at 80 °C for 1 h.

Bottom cover slip with a microtrack array. An aluminium layer was deposited on a borosilicate cover slip (24 × 36 mm, no. 1 thickness, Matsunami) after cleaning in piranha solution (mixture of sulphuric acid and hydrogen peroxide, 3:1 (v/v)). The thickness of aluminum layer was monitored during thermal deposition until a thickness of ~150 nm was obtained. An SU-8 2000.5 resist (MicroChem) was then spin-coated (1H-D7, Mikasa) and patterned using a double-sided mask aligner (PEM800, Union). An array of microtracks (2 μm in width in the design) was fabricated by developing an SU-8 layer in an SU-8 developer (MicroChem) and etching the aluminum layer. The width of the etched microtracks was measured to be 2.1 ± 0.1 μm (mean ± SD) from microscope images. The total height of the aluminum and SU-8 layers was 0.7 ± 0.07 μm, which was measured using a surface profilometer. Etching was implemented immediately before device assembly to utilise the clean glass surface for uniform immobilisation of kinesin. This is because we found that some MTs did not glide smoothly when the cover slip was stored for >2 days after the aluminium etching process.

Device assembly. The top PDMS layer was first bonded to the middle PDMS layer after exposure to air plasma (Covance MP, Femto Science). The middle PDMS layer remained attached to the silicon wafer; bonding was completed by curing for 1 h at 80 °C. The two bonded PDMS layers were then peeled from the fluidic channel mould. Holes of 3 mm diameter were punched in the PDMS slab to serve as the solution inlet and outlet, and the slab was bonded to the bottom glass cover slip activated by exposure to air plasma. Finally, the device was cured for 1 h at 80 °C to reduce the prepolymers, which remained uncured, and reinforce the bonding strength. Control channels were connected to an external pressure source, and the supply of pressure was individually controlled through each channel by using an electromagnetic valve with a digital regulator (ARP20K-02, SMC). Before applying pressure, the PDMS membrane on top of the microchannel array was not deformed (Fig. 1d-1). Once 100 kPa of pressure was applied to the control channel, the membrane in the middle PDMS layer was deformed to seal the top of the microtracks fabricated on the bottom cover slip (Fig. 1d-2).

Protein preparation

The kinesin construct consisted of sequence-encoding human kinesin amino acid residues 1–573 with a 6-residue N-terminal

histidine tag, which was purified by chelating to a nickel-coupled resin, as described.[49] Tubulin was purified from porcine brain, as described,[50] which yielded 5–6 mg mL^{-1} tubulin solution. Purified tubulin was fluorescently labelled by conjugating with tetramethyl rhodamine (C1171, Molecular Probes). Kinesin, tubulin, and fluorescently labelled tubulin were aliquoted into sample tubes and stored in liquid nitrogen. Labelled MTs were polymerised by mixing non-labelled tubulin and labelled tubulin at a molar ratio of 10:1 at 37 °C for 45 min in the presence of 0.5 mM MgSO$_4$ and 0.5 mM GTP. A solution containing polymerised MT solution was stored at room temperature after adding 4 μM Taxol as a stabilising agent and was used within one week.

Motility assay

Before starting the assay, the device was degassed in a vacuum chamber for 1 h. Assay solutions were sequentially introduced into the assay channel with valve operations to achieve selective immobilisation of proteins in the target area (Fig. 2a). Immediately after the device was removed from the chamber, fluid inlet and outlet holes were filled with 2 mg mL^{-1} Pluronic F108 (BASF) solution with all valves 1–5 open (Fig. S3a†). The solution was autonomously introduced into fluidic channels by applying negative pressure, and then Pluronic F108 was rinsed out with BRB80 buffer (80 mM PIPES, 1 mM EGTA, 1 mM MgSO$_4$, pH 6.8) for >3 min. The flow was regulated by the head difference (~5 mm) between the fluid inlet and outlet. Kinesin solution, diluted to 70 μg mL^{-1} in BRB80 containing 0.2 mg mL^{-1} casein, was then introduced via the fluid inlet (Fig. S3b†). To ensure kinesin immobilisation, the flow was maintained for 10 min followed by 3 min incubation by closing valves 1 and 4 (Fig. S3c†). The kinesin solution was washed out by flowing BRB80 for 3 min with valves 1, 4, and 5 open (Fig. S3d†). Valves 4 and 5 were closed before MT solution was introduced to immobilise MTs only in area 1 (Fig. 2b, c and S3e†). The MT solution was prepared using a tubulin dimer concentration of 120 μg mL^{-1} in BRB80 containing 1 mM ATP, 4 μM Taxol, and an oxygen scavenging system (36 μg mL^{-1} catalase, 25 mM glucose, 216 μg mL^{-1} glucose oxidase, 1% β-mercaptoethanol, 0.2 mg mL^{-1} casein, and 20 mM dithiothreitol). At this stage, we have confirmed that no MTs were introduced into the channel array or area 2 by pressure-driven flow (Fig. 2d) and observed that MTs started gliding. During the assay, fluid flow was continuously supplied to area 1 by opening valves 1 and 3, while flow in area 2 was stopped by closing valve 4 (Fig. S3e†). Valve 2 was kept open to avoid imbalance of pressure.

Stable MT motility by supplying N$_2$

N$_2$ was supplied via two N$_2$ inlets and vented via two outlets as indicated by green arrows in Fig. 1a. Gas flow was supplied for 30 min before starting the assay and was maintained during the assay. Gas pressure was maintained at 10 kPa, which was substantially lower than the pressure required to control the valve (~100 kPa), so as to avoid unexpected closure or deformation of the fluidic channels.

Imaging and data processing

Gliding of labelled MTs and Brownian motion of quantum dots (Q-dots) (Q10121MP, Invitrogen) were visualised via fluorescence microscopy (IX 71, Olympus), in which 40× and 100× objective lenses were used for MT and Q-dot observations, respectively. Images were recorded using an electron multiplying charge-coupled device camera (iXon EM+ DU-897, Andor Technology PLC) connected to a PC. An exposure time of 400 ms, an electron-multiplying gain of 299 and a neutral density filter (6% transmission) were used throughout the MT assay. MT velocities were measured using Mark II software.[51] MTs were counted using ImageJ (National Institute of Health) and Lines8 plugin.

When the Brownian motion of Q-dots was observed in the microchannel array, the exposure time was reduced to 10 ms for higher temporal resolution. Q-dots were tracked from sequential TIFF images using FIESTA software[52]. The obtained trajectories were further analysed with MatLab 2013b (MathWorks).

Results and discussion

Dynamic formation of the microchannel array

Complete closure of the channel array was verified by observing the Brownian motion of Q-dots (1 nM). In the area where the top of the microtrack array was not closed by the PDMS
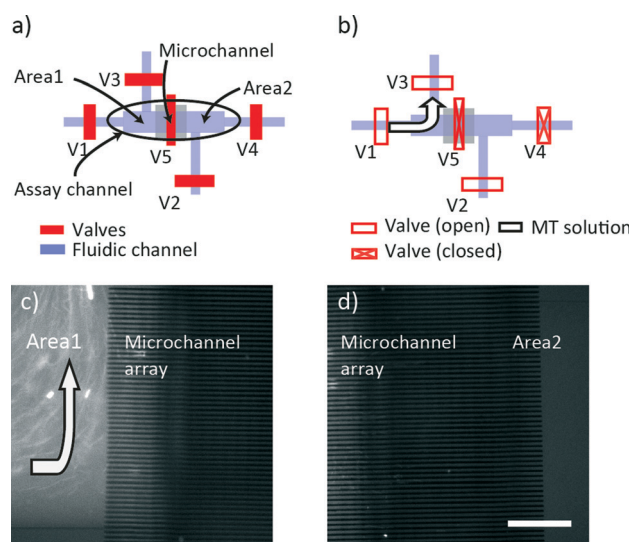

Fig. 2 Selective injection of buffer solutions by actuating pneumatic valves. a) Schematic of the flow control. Liquid flow to the assay channel is controlled by four valves (valves 1–4). Valve 5 forms the microchannel array. b) Upon introduction of MT solution, valves 4 and 5 are closed to selectively introduce MTs into area 1. c) MT introduction. MTs were selectively introduced into area 1, but not into the microchannel array. Flow direction is visualised by aligned MTs in the flow direction indicated by the white arrow. d) MTs were not observed in the microchannel area and area 2 because MT diffusion was suppressed by valve operation. Scale bar is 50 μm.

membrane (blue rectangle area in Fig. 3a), the Brownian motion of Q-dots was restricted within the track width but not in the out-of-plane direction (z-axis direction) (ESI† Movie 2). This resulted in a short residence time of the Q-dots in the viewing area (blue trajectories in Fig. 3a). On the other hand, the Q-dots in the microchannel array where the PDMS membrane was compressed showed Brownian motion restricted in both the in-plane and out-of-plane directions (red rectangle area in Fig. 3a). Therefore, the red trajectories in Fig. 3a were longer than the blue ones.

Q-dot confinement was quantified. The residence time of Q-dots (i.e., the frame number continuously tracked) was measured and is plotted in Fig. 3b. Apparently, the Q-dots in the microchannel array (red) showed longer residence time than those in the microtrack array (blue). Q-dot tracking was terminated, once the Q-dots escaped from the focal depth. Therefore, when Q-dot diffusion was suppressed in the microchannel array, the probability that a Q-dot was observable in two consecutive frames increased. In Fig. 3b, we plotted a histogram of residence time (or frame number; one frame corresponds to 0.043 s) measured from Q-dot trajectories in the microtrack and microchannel arrays. As the residence time is stochastically determined, the histograms are fitted by exponential decay (Fig. 3b) expressed as:

$$N_i = N_0 p^{(i-1)}, \qquad (1)$$

where p is the probability that a Q-dot is continuously observed in two frames, i is the frame number, and N_0 is the normalisation factor. Curve fitting to histograms yielded p values of 0.38 and 0.69 for Q-dots in the microtrack and microchannel arrays, respectively. This significant difference in residence time demonstrated that the probability of Q-dot confinement increased in the out-of-plane direction. In addition, of the 688 Q-dots tracked in the microchannel array, 10 could be observed in more than 20 consecutive frames, corresponding to 1.5% of all the Q-dots. The ratio (1.5%) is $>10^6$ times larger than that calculated for a Q-dot exposed to three-dimensional diffusion. These analyses strongly indicate that Q-dot diffusion in the out-of-plane direction was limited by the dynamic formation of the microchannel array.

Q-dot confinement was also evaluated by time development of the mean squared displacement (MSD) of each Q-dot trajectory along the x and y axes defined in Fig. 3a. Two average MSDs in x and y directions are plotted in Fig. 3c, which were calculated from all the trajectories at each time point. Because the residence time varied, as shown in Fig. 3b, the number of trajectories used for MSD calculation decreased with elapsed time. For example, MSDs were calculated from 688 trajectories at time = 0 s and from 5 trajectories at time = 1.4 s. In addition, the theoretical MSD calculated for diffusion was also plotted. The y-MSD curve showed a continuous increase, but the x-MSD curve did not increase appreciably over time. The trend of the y-MSD was relatively small compared to that of the theoretical plot (see the ESI† for details). This discrepancy can be explained by the hindrance of particle diffusion near the surface. In the condition where the distance between a particle and a surface is relatively small compared to the particle radius, the diffusion coefficient decreases as a function of the ratio. Assuming that the ratio is around 0.2 (10 nm (Q-dot radius)/ 50 nm (the distance) for our experimental setup), the diffusion coefficient is reported to drop ~80% of that in free diffusion.[53] The inset in Fig. 3c shows an enlargement of the period 0–0.4 s. The observed small MSD along the x direction, which is perpendicular to the channel, indicates confinement of Q-dots in the channel. Both residence time and MSD analyses quantitatively proved that the microchannel array was indeed completely sealed upon its formation after actuation of the PDMS membrane.
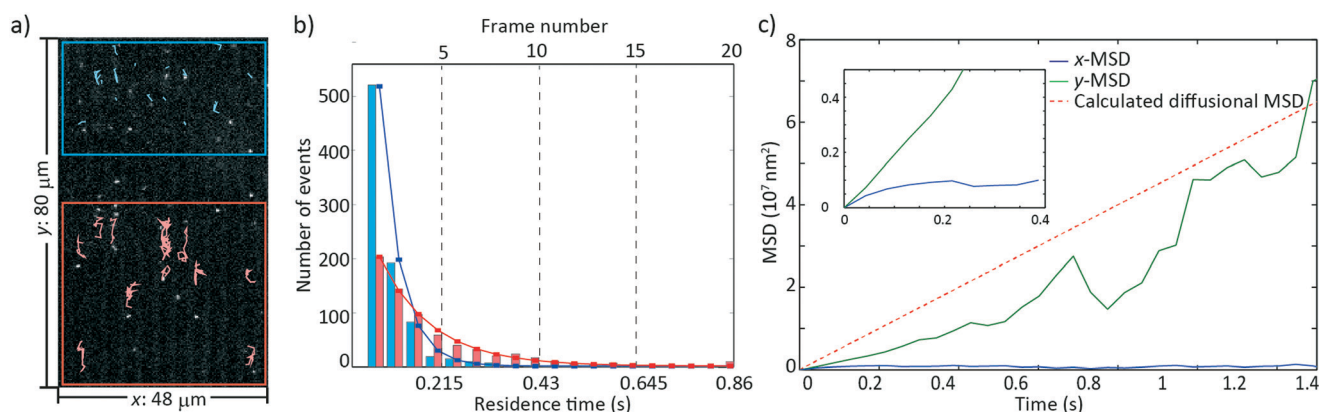

Fig. 3 Evaluation of channel closure. a) Trajectories of Q-dots by Brownian motion. The area enclosed by the blue rectangle corresponds to the microtrack array, i.e., the PDMS membrane is not compressed, where Q-dot trajectories are shown in blue. The microchannel array was formed in the red rectangle area, where Q-dot trajectories are in red. b) Residence time histogram for trajectories obtained in the microtrack array (blue) and the microchannel array (red). The total number of trajectories was 868 and 688 in the microtrack and microchannel arrays, respectively. c) Plots of MSDs. Time course of MSDs along the x and y directions was calculated from Q-dot trajectories in the microchannel array. Inset is an enlarged view of MSDs from 0 s to 0.4 s. y-MSD (green) increased over time and showed a trend similar to that of the MSD theoretically calculated for free diffusion (red dotted line). However, x-MSD (blue) remained nearly zero.
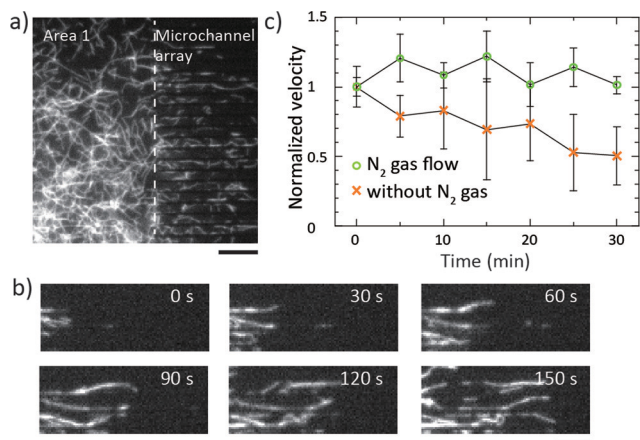
Fig. 4 MT motility in the microchannel array with N_2 flow. a) Overview of gliding MTs in the area 1 side of the microchannel array. Scale bar is 10 μm. b) Sequential images of gliding MTs. Scale bar is 5 μm. c) Time course of gliding velocity with (closed circle) and without (cross) N_2 flow. Error bars represent the standard deviation of the average calculated from more than five MTs.

Preservation of gliding motility in assay channels by N_2 flow

In our first trial of the assay in the PDMS device, we noticed that the MT velocity drastically decreased after 10–15 min. We attributed this to the high oxygen gas (O_2) permeability of PDMS since Brunner *et al.* reported the deceleration of MTs in <30 s on a PDMS surface under fluorescence excitation due to damage to both kinesin and MT molecules by reactive oxygen species.[54] Fortunately, an N_2 gas chamber system can preserve MT gliding motility for >10 min in a PDMS flow cell,[55,56] and it has been recently reported that photodamage

can be minimized in a PDMS microfluidic device by using an N_2 stream to purge O_2 gas from the PDMS.[57] Therefore, to purge O_2 gas from the PDMS surrounding the assay area, we delivered N_2 through control channels as described in Materials and methods. MT gliding was observed in area 1, and some MTs glided into the microchannel array (Fig. 4a, b). The effect of the method was quantified by measuring the MT velocity with or without N_2 flow. The time course of velocity v was normalised by the initial velocity v_i and is plotted in Fig. 4c. Without N_2 flow, the normalised velocity decreased from the initial 1.0 ± 0.14 (v/v_i) (mean ± SD) to 0.50 ± 0.2 (v/v_i) after 30 min. In contrast, the MT velocity with N_2 flow did not decrease significantly over 30 min, resulting in an essentially constant normalised velocity of 1.0 ± 0.1 (v/v_i). These results demonstrate the general applicability of the proposed method for the MT assay in any PDMS-based device.

Transport of MTs through the microchannel array

In our initial assays, MTs were first introduced into area 1 only by selective valve operation, and MTs were not observed in area 2 (Fig. 2b, c and S3d†). Many MTs were found on the left (area 1) side of the array at $t = 180$ s and gradually translocated into the right side (area 2, Fig. 5a). This was also captured as a movie clip (ESI† Movie 1). This MT motility could not be achieved without valve operation because unbound MTs were observed in the conventional flow cell-based assay. Fig. 5b and c show the fluorescence intensity profile along each of the two lines A–B (180 s) and A'–B' (720 s) in Fig. 5a. No fluorescence intensity peak, *i.e.*, corresponding to a MT, was detected at 180 s, whereas many peaks were observed at 720 s.
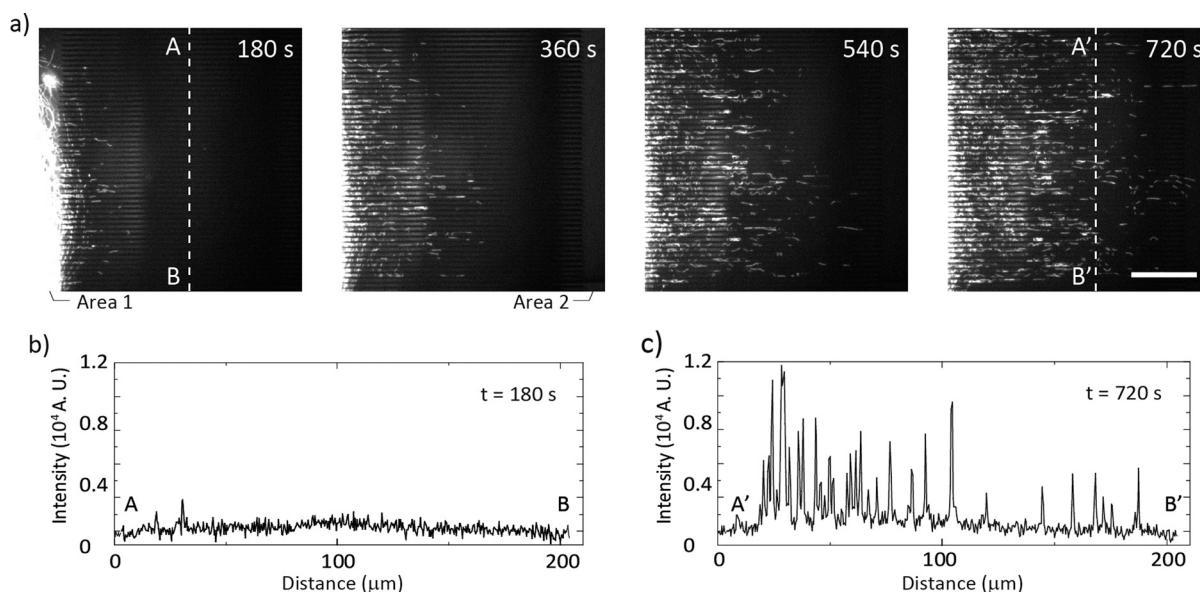

Fig. 5 Transition of MT distribution in the microchannel array over time. a) Sequential images of MTs transiting from area 1 to area 2. After starting the assay, a few MTs glided into microchannels at 180 s. Several MTs reached area 2 at 540 s. More MTs were found in area 2 at 720 s. Scale bar is 50 μm. Fluorescence intensity profile (arbitrary unit, A. U.) along A–B at b) 180 s and A'–B' at c) 720 s. Many peaks were observed in (c) due to the presence of MTs in the microchannel array.

To further evaluate transition time of MTs, we measured the time-course change in MT density in the two regions demarcated by orange rectangles in the insets of Fig. 6a and b. The former region corresponds to the area where the microchannel array was formed, and the latter is located in area 2 (exit of the channels). In Fig. 6a, the MT density was nearly zero at $t = 0$ s and increased until the density reached a maximum. The increase can be explained by the fact that the MTs moved from area 1 into the microchannel array where MTs were not initially present. Once the microchannel array was filled with MTs and the numbers of incoming and outgoing MTs were balanced, the MT density was maximal. Based on this idea, the time course of the MT density, D_{MT}, was fitted by the equation:

$$D_{MT}(t) = \begin{cases} kt & (t < T) \\ kT & (t \geq T) \end{cases}, \tag{2}$$

where k represents the coefficient of the increase in D_{MT}, and T is the time needed to achieve maximal MT density. T was calculated to be 6.2×10^2 s by least squares fitting.

Fig. 6b shows the time course of the MT density in area 2. MTs were not observed in area 2 until $t = 700$ s. The time-course of D_{MT} was fitted by the equation:

$$D_{MT}(t) = \begin{cases} 0 & (t < T') \\ k'(t - T') & (t \geq T') \end{cases}, \tag{3}$$

where k' is the coefficient of the increase in D_{MT} and T' is the time when the density begins to increase. The values of T' and k' were calculated to be 650 s and 1.1×10^{-5} µm^{-2} s^{-1}, respectively. Fitted values, k, T, k' and T', can be used to evaluate the transport effectiveness of the system. For example, the increase rate of MTs in the region of 40.0×205 µm (orange rectangle, Fig. 6b) was calculated to be 9.3×10^{-2} s^{-1}.

This increase in MT density could not be realised without controlling the pressure difference between areas 1 and 2. If this pressure difference was larger than that between valves 1 and 2 (see Fig. 2a and b), selective introduction of MT solution into area 1 would be perturbed. For the sake of practicality, the average flow velocity induced by a pressure difference in the channels was calculated by using the Darcy–Weisbach equation.[58] For example, assuming that the pressure difference between areas 1 and 2 was 10 Pa, the average velocity in the microchannel array was calculated to be 6.2 µm s^{-1}. On the other hand, when the microtrack array was not closed by the PDMS membrane, the average velocity under the same pressure difference was calculated to be 3.8 mm s^{-1} (see the ESI† for details). This comparison of flow velocities indicates that the microchannel array can serve as a barrier to avoid cross-contamination during solution exchange.

Analysis of active transport and comparison with *in vivo* transport

Compared with the free diffusion of molecules, molecular shuttling—as represented by the active transport of MTs by kinesin—can achieve enhanced and directed transport in microfluidic environments.[11,59] Here, we applied the same idea to our microfluidic device; we calculated the time required to equilibrate the concentrations of MTs in the two areas (compartments) connected by the channel array. Assuming a molecular diameter of 10 nm, area 1 (0.2 nL, 20 µm × 100 µm × 100 µm) was filled with a 1 nM solution of molecules, and area 2 (same volume as area 1) was free of molecules; in this scenario, diffusion-driven transport displaced ~3000 molecules (see the ESI† for details) from area 1 into area 2 within 10 min, which is equivalent to 2.5% of all molecules. When active transport was employed, however, the same number of molecules was transported from area 1 into area 2 in the initial ~100 s. Here, we assumed that MTs served as cargo transporters[12,60] and ~30 cargo molecules were carried on a 10 µm-long MT per second (see the ESI† for details). This comparison clearly indicates that active transport of molecules, rather than their simple diffusion, predominated in the proposed device. This advantage would
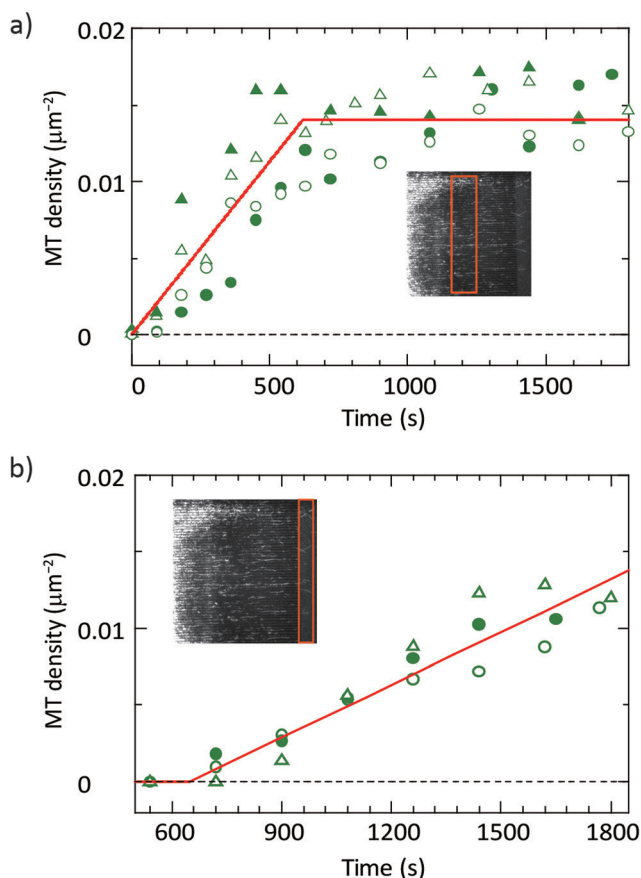
Fig. 6 MT density as a function of time. a) MT density in the microchannel area. MTs were counted within the area enclosed by the orange rectangle. Data in the plots were obtained from four experiments, and curve fitting yielded the red line. b) MT density in area 2 was measured by counting the number of MTs within the area enclosed by the orange rectangle. Data were obtained from three experiments and were fitted as noted for panel a.

be further enhanced if target molecules were larger or the solution viscosity was greater, because these parameters result in a smaller diffusion coefficient, yielding a slower rate of transport. This simple calculation demonstrates how active transport potentiates the utility of microfluidic devices.

Conclusion

Here, we realised transitional and unidirectional transport of MTs from a MT-supplied area (area 1) into a MT-free area (area 2) that are physically separated in the microfluidic device. One essential function of the device was to utilise a PDMS membrane to dynamically form the microchannel array from the microtrack array, which was examined by analysis of Q-dot Brownian motion. Another essential function was to suppress photobleaching of MTs by delivering N_2 flow through control channels.

Toward sequential molecular analysis utilising MTs as molecular shuttles, the device provides the advantage of handling target molecules between adjacent compartments without the help of continuous laminar flow. It allows us to focus on the active transport of MTs. Because the assay was validated in an integrated PDMS microfluidic device, the method has further potential to take advantage of the properties of PDMS to achieve higher productivity, cost efficiency, and integration with microfluidic components such as peristaltic pumps.[61] The proposed experimental system constitutes a substantial advance in the development of practical nano/micro-scale fluidic devices driven by motor proteins.

Acknowledgements

Notes and references

1 A. Manz, N. Graber and H. M. Widmer, *Sens. Actuators, B*, 1990, **1**, 244–248.

2 H. A. Stone, A. D. Stroock and A. Ajdari, *Annu. Rev. Fluid Mech.*, 2004, **36**, 381–411.

3 A. Arora, G. Simone, G. B. Salieb-Beugelaar, J. T. Kim and A. Manz, *Anal. Chem.*, 2010, **82**, 4830–4847.

4 J. Fu, R. B. Schoch, A. L. Stevens, S. R. Tannenbaum and J. Han, *Nat. Nanotechnol.*, 2007, **2**, 121–128.

5 D. W. Inglis, E. M. Goldys and N. P. Calander, *Angew. Chem.*, 2011, **123**, 7688–7692.

6 C. L. Zhao and C. Yang, *Microfluid. Nanofluid.*, 2012, **13**, 179–203.

7 A. Goel and V. Vogel, *Nat. Nanotechnol.*, 2008, **3**, 465–475.

8 M. A. Welte, *Curr. Biol.*, 2010, **20**, R410–413.

9 E. Nogales, *Annu. Rev. Biochem.*, 2000, **69**, 277–302.

10 T. Korten, A. Månsson and S. Diez, *Curr. Opin. Biotechnol.*, 2010, **21**, 477–488.

11 H. Hess and V. Vogel, *Rev. Mol. Biotechnol.*, 2001, **82**, 67–85.

12 C. Schmidt, B. Kim, H. Grabner, J. Ries, M. Kulomaa and V. Vogel, *Nano Lett.*, 2012, **12**, 3466–3471.

13 C. Schmidt and V. Vogel, *Lab Chip*, 2010, **10**, 2195–2198.

14 R. Yokokawa, J. Miwa, M. C. Tarhan, H. Fujita and M. Kasahara, *Anal. Bioanal. Chem.*, 2008, **391**, 2735–2743.

15 S. Hiyama, Y. Moritani, R. Gojo, S. Takeuchi and K. Sutoh, *Lab Chip*, 2010, **10**, 2741–2748.

16 M. Lard, L. ten Siethoff, J. Generosi, A. Månsson and H. Linke, *Nano Lett.*, 2014, **14**, 3041–3046.

17 G. D. Bachand, S. B. Rivera, A. Carroll-Portillo, H. Hess and M. Bachand, *Small*, 2006, **2**, 381–385.

18 L. Rios and G. D. Bachand, *Lab Chip*, 2009, **9**, 1005–1010.

19 S. Ramachandran, K.-H. Ernst, G. D. Bachand, V. Vogel and H. Hess, *Small*, 2006, **2**, 330–334.

20 H. Hess, J. Clemmens, D. Qin, J. Howard and V. Vogel, *Nano Lett.*, 2001, **1**, 235–239.

21 H. Hess, C. M. Matzke, R. K. Doot, J. Clemmens, G. D. Bachand, B. C. Bunker and V. Vogel, *Nano Lett.*, 2003, **3**, 1651–1655.

22 Y. Hiratsuka, T. Tada, K. Oiwa, T. Kanayama and T. Q. Uyeda, *Biophys. J.*, 2001, **81**, 1555–1561.

23 S. G. Moorjani, L. Jia, T. N. Jackson and W. O. Hancock, *Nano Lett.*, 2003, **3**, 633–637.

24 J. Clemmens, H. Hess, R. Doot, C. M. Matzke, G. D. Bachand and V. Vogel, *Lab Chip*, 2004, **4**, 83–86.

25 T. Kim, M.-T. Kao, E. F. Hasselbrink and E. Meyhöfer, *Nano Lett.*, 2007, **7**, 211–217.

26 M. Uppalapati, Y.-M. Huang, V. Aravamuthan, T. N. Jackson and W. O. Hancock, *Integr. Biol.*, 2011, **3**, 57–64.

27 M. G. L. van den Heuvel, C. T. Butcher, S. G. Lemay, S. Diez and C. Dekker, *Nano Lett.*, 2005, **5**, 235–241.

28 N. Isozaki, S. Ando, T. Nakahara, H. Shintaku, H. Kotera, E. Meyhöfer and R. Yokokawa, *Sci. Rep.*, 2015, **5**, 7669–7669.

29 B. M. Hutchins, M. Platt, W. O. Hancock and M. E. Williams, *Small*, 2007, **3**, 126–131.

30 T. Kim, M.-T. Kao, E. Meyhöfer and E. F. Hasselbrink, *Nanotechnology*, 2007, **18**, 025101.

31 R. Yokokawa, S. Takeuchi, T. Kon, M. Nishiura, K. Sutoh and H. Fujita, *Nano Lett.*, 2004, **4**, 2265–2270.

32 R. R. Agayan, R. Tucker, T. Nitta, F. Ruhnow, W. J. Walter, S. Diez and H. Hess, *Langmuir*, 2013, **29**, 2265–2272.

33 L.-J. Cheng, M.-T. Kao, E. Meyhöfer and L. J. Guo, *Small*, 2005, **1**, 409–414.

34 C. Reuther, L. Hajdo, R. Tucker, A. A. Kasprzak and S. Diez, *Nano Lett.*, 2006, **6**, 2177–2183.

35 M. Bhagawati, S. Ghosh, A. Reichel, K. Froehner, T. Surrey and J. Piehler, *Angew. Chem., Int. Ed.*, 2009, **48**, 9188–9191.

36 T. Fischer, A. Agarwal and H. Hess, *Nat. Nanotechnol.*, 2009, **4**, 162–166.

37 C.-T. Lin, M.-T. Kao, K. Kurabayashi and E. Meyhofer, *Nano Lett.*, 2008, **8**, 1041–1046.

38 G. D. Bachand, H. Hess, B. Ratna, P. Satir and V. Vogel, *Lab Chip*, 2009, **9**, 1661–1666.

39 T. Kim, L.-J. Cheng, M.-T. Kao, E. F. Hasselbrink, L. Guo and E. Meyhöfer, *Lab Chip*, 2009, **9**, 1282–1285.

40 D. Steuerwald, S. M. Früh, R. Griss, R. D. Lovchik and V. Vogel, *Lab Chip*, 2014, **14**, 3729–3738.

41 M. A. Unger, H. P. Chou, T. Thorsen, A. Scherer and S. R. Quake, *Science*, 2000, **288**, 113–116.

42 M. Nagai, S. Ryu, T. Thorsen, P. Matsudaira and H. Fujita, *Lab Chip*, 2010, **10**, 1574–1578.

43 Y.-M. Huang, M. Uppalapati, W. O. Hancock and T. N. Jackson, *Biomed. Microdevices*, 2007, **9**, 175–184.

44 M. G. L. van den Heuvel, M. P. de Graaff and C. Dekker, *Science*, 2006, **312**, 910–914.

45 M. Uppalapati, W. O. Hancock and T. N. Jackson, *IEEE Trans. Adv. Packag.*, 2005, **28**, 564–570.

46 R. Yokokawa, Y. Yoshida, S. Takeuchi, T. Kon and H. Fujita, *Nanotechnology*, 2006, **17**, 289–294.

47 A. M. R. Kabir, D. Inoue, A. Kakugo, K. Sada and J. P. Gong, *Polym. J.*, 2012, **44**, 607–611.

48 Y. Q. Luo and R. N. Zare, *Lab Chip*, 2008, **8**, 1688–1694.

49 R. Yokokawa, M. C. Tarhan, T. Kon and H. Fujita, *Biotechnol. Bioeng.*, 2008, **101**, 1–8.

50 R. C. Williams and J. C. Lee, *Methods Enzymol.*, 1982, **85**, 376–385.

51 K. Furuta, A. Furuta, Y. Y. Toyoshima, M. Amino, K. Oiwa and H. Kojima, *Proc. Natl. Acad. Sci. U. S. A.*, 2013, **110**, 501–506.

52 F. Ruhnow, D. Zwicker and S. Diez, *Biophys. J.*, 2011, **100**, 2820–2828.

53 B. Lin, J. Yu and S. Rice, *Phys. Rev. E: Stat. Phys., Plasmas, Fluids, Relat. Interdiscip. Top.*, 2000, **62**, 3909–3919.

54 C. Brunner, K. Ernst, H. Hess and V. Vogel, *Nanotechnology*, 2004, **15**, S540–S548.

55 R. M. Lycans, C. B. Higgins, M. S. Tanner, E. R. Blough and B. S. Day, *Colloids Surf., B*, 2014, **116**, 687–694.

56 A. M. R. Kabir, D. Inoue, A. Kakugo, A. Kamei and J. P. Gong, *Langmuir*, 2011, **27**, 13659–13668.

57 V. Vandelinder and G. D. Bachand, *Anal. Chem.*, 2014, **86**, 721–728.

58 N.-T. Nguyen and S. T. Wereley, *Fundamentals and Applications of Microfluidics*, Artech House, Norwood, MA, 2002.

59 P. Katira and H. Hess, *Nano Lett.*, 2010, **10**, 567–572.

60 G. D. Bachand, S. B. Rivera, A. K. Boal, J. Gaudioso, J. Liu and B. C. Bunker, *Nano Lett.*, 2004, **4**, 817–821.

61 C.-H. Wang and G.-B. Lee, *J. Micromech. Microeng.*, 2006, **16**, 341–348.